Research Article

Exploring the oxygen vacancies and electrical properties in pyrochlore-type $Ca_{1.46}Ti_{1.38}Nb_{1.11}O_7$

Yuan Yao, Shuhang Liu, Heyuan Sun, Jiajia Yao, Wen-Cui Li, Wenrui Zhang*

State Key Laboratory of Fine Chemicals, School of Chemical Engineering, Dalian University of Technology, Dalian 116024, Liaoning, China.

***Correspondence to:** Prof. Wenrui Zhang, State Key Laboratory of Fine Chemicals, School of Chemical Engineering, Dalian University of Technology, Dalian 116024, Liaoning, China. E-mail: zhangwr@dlut.edu.cn

ORCID: Wenrui Zhang (0000-0003-1590-534X)

How to cite this article: Yao Y, Liu S, Sun H, Yao J, Li WC, Zhang W. Exploring the oxygen vacancies and electrical properties in pyrochlore-type $Ca_{1.46}Ti_{1.38}Nb_{1.11}O_7$. *Microstructures* 2026;6:[Accept]. http://dx.doi.org/10.20517/microstructures.2026.08

Received: 14 January 2026 | **Revised:** 17 March 2026 | **Accepted:** 26 March 2026

Abstract

Pyrochlore-type oxides are considered potential oxide-ion conductors due to their high concentration of oxygen vacancies in the unit cell. In this work, the pyrochlore-type $Ca_{1.46}Ti_{1.38}Nb_{1.11}O_7$ was synthesized and its crystal structure was characterized by Rietveld refinement. A high oxygen vacancy concentration in the material was confirmed by thermogravimetry (TG) and X-ray photoelectron spectroscopy (XPS). TG, XPS, and electron paramagnetic resonance (EPR) collectively demonstrated the change in oxygen vacancy concentration of the material following atmosphere switching. The electrical properties of $Ca_{1.46}Ti_{1.38}Nb_{1.11}O_7$ under different atmospheres were characterized by electrochemical impedance spectroscopy. The conductivity of $Ca_{1.46}Ti_{1.38}Nb_{1.11}O_7$ was 4.20×10^{-2} S cm^{-1} in 5%

H_2/Ar, 9.22 × 10^{-3} S cm^{-1} in Ar and 2.92 × 10^{-5} S cm^{-1} in air at 900 ℃. Bond valence site energy calculations indicated that oxide ions diffuse three-dimensionally in $Ca_{1.46}Ti_{1.38}Nb_{1.11}O_7$. $Ca_{1.46}Ti_{1.38}Nb_{1.11}O_7$ is a promising solid electrolyte for oxygen sensors. This work investigates the structure-property relationship between oxygen vacancies and conductivity in pyrochlore-type oxides.

Keywords: Ionic conductor, conductivity, solid electrolyte, solid oxide fuel cells, ion migration

INTRODUCTION

Since Nernst's discovery of oxide-ion conduction in Y_2O_3-ZrO_2, the field has advanced significantly, and oxide-ion conductors now play a vital role in daily life and industrial applications[1-4]. Oxide-ion conductors have found extensive applications as catalytic, sensing, and conductive materials under various atmospheres, including oxidizing, reducing, inert, and mixed environments. High-performance oxide-ion conductors are key materials for enabling efficient operation in solid-state electrochemical devices, such as solid oxide fuel cells and oxygen sensors[5].

In addition to the charge carrier (e.g. oxygen vacancies or interstitial oxygen ions) concentration, the local crystalline structure around the charge carrier is a crucial factor for oxide-ion conduction[6]. Most of the conventional oxide-ion conductors are fluorite-type materials, such as yttria-stabilized zirconia (YSZ) and Gd- or Sm-doped CeO_2 (GDC or SDC), the structure of which can provide large tolerances for disordered oxygen vacancies[7-10]. The pyrochlore structure is an intricate superstructure derived from the fluorite structure and inherently contains more oxygen vacancies[11]. Pyrochlore-type oxides have attracted high attention for a long time due to their potential applications such as thermal barrier coating materials, solid electrolytes, oxygen pumps, oxygen sensors, catalysts, and so on[12, 13].

The typical pyrochlore structure consists of two types of cations, *A* and *B*, occupying different lattice sites, where *A*-site cations are larger and usually have a lower oxidation state, while *B*-site cations are smaller and have a higher oxidation state[14]. The *A*-site cations occupy the centers of oxygen octahedra, whereas the *B*-site cations, typically transition metals, reside within them[14]. Partial substitution of *A*-site or

B-site ions with other metal ions not only disrupts the structural ordering of the pyrochlore lattice but also alters the unit cell size, thereby potentially decreasing the oxide-ion migration distance[15]. The presence of numerous oxygen vacancies in pyrochlore-type oxides is beneficial for oxide-ion conduction, as it provides pathways for ion migration[16]. The pyrochlore structure's coordination environment allows for diverse cationic configurations, supporting multiple oxidation states[17-19]. This structural arrangement, combined with its capability to incorporate a wide range of ions, significantly enhances the physical and chemical stability, making pyrochlore-type oxides suitable for use as oxide-ion conductors[20-26].

R.S. Roth et al.[27] reported the pyrochlore-type $Ca_{1.46}Ti_{1.38}Nb_{1.11}O_7$ and investigated its dielectric properties. Bond valence site energy (BVSE) calculations performed with the softBV software[28-30] indicate that the material exhibits a relatively low oxide-ion migration barrier (1.14 eV), suggesting its potential as an oxide-ion conductor. This work aims to investigate the conductive properties of $Ca_{1.46}Ti_{1.38}Nb_{1.11}O_7$ and elucidate its oxide-ion conduction mechanism. In particular, it seeks to clarify the structure-property relationship between oxygen vacancies and conductivity, as well as the formation mechanism of oxygen vacancies. The findings are expected to provide insights for future research on pyrochlore-type oxides.

EXPERIMENTAL PROCEDURE

Material synthesis

$Ca_{1.46}Ti_{1.38}Nb_{1.11}O_7$ was synthesized using a solid-state reaction method. High-purity $CaCO_3$, TiO_2 and Nb_2O_5 powders (≥ 99.9%, Aladdin Biochemical Technology Co., Ltd., China) were used as starting materials, which were dried in an oven (DHG-9075A, Yiheng Scientific Instrument Co., Ltd., China) to remove adsorbed water prior to weighing. The starting materials were ground in anhydrous ethanol (AR, ≥ 99.7%, Sinopharm Chemical Reagent Co., Ltd., China) for approximately 30 min. The mixtures were pressed into pellets and pre-sintered at 1000 ℃ for 12 h, and then sintered at 1350 ℃ for 8 h. The sintered sample was ground, pressed into pellets, and finally sintered at 1350 ℃ for 8 h for densification. All sintering processes were carried out in Ar gas (≥ 99.999%, Dalian Special Gases Co., Ltd., China) using a horizontal tube furnace (GYS-1700C, Hefei Weiyuans Laboratory Equipment Co., Ltd., China).

Material characterization

The X-ray diffraction (XRD) pattern was obtained using a powder diffractometer (X'Pert3 Powder, PANalytical, The Netherlands) with Cu $K\alpha$ radiation. Rietveld refinement and Maximum Entropy Method (MEM) analysis were carried out using the Z-Rietveld software. BVSE calculations were performed using the softBV program to calculate the oxide-ion migration barriers. Visualization of the results was achieved using VESTA software. The elemental composition of the sample was determined by X-ray fluorescence spectrometry (XRF) using a wavelength-dispersive spectrometer (S8 Tiger, Bruker, Germany). Field emission scanning electron microscopy (SEM) (JSM-7900F, JEOL Ltd., Japan) equipped with energy-dispersive X-ray spectroscopy (EDS) was employed to investigate the morphology of the pellet samples and the elemental distribution of the powder samples. The particle size distribution of the sample was determined using a laser particle size analyzer (BT-9300H, Dandong Bettersize Instruments Co., Ltd., China). For electrochemical impedance spectroscopy measurements, pellets (approximately 10 mm in diameter and 2 mm in thickness) were used. Platinum paste electrodes (55H-1800, Shenzhen Saiya Electronic Paste Co., Ltd., China) were coated on its opposite faces. The sample was then heated at 1000 ℃ for 2 h in a horizontal tube furnace (GYS-1700C, Hefei Weiyuans Laboratory Equipment Co., Ltd., China) to form dense platinum electrodes. Electrochemical measurements were performed on an electrochemical workstation (SP-300, Bio-Logic, France; or DH7002A, Donghua Analytical Instrument Co., Ltd., China) using the two-electrode method during the heating process. The sample was heated to temperatures between 500 °C and 900 °C in either a tubular furnace (JS-G5012-S, Tianjin Jiusuo Technology Development Co., Ltd., China) or a solid oxide fuel cell test station (HBSOC-5B, Zhejiang H_2-Bank Energy Technology Co., Ltd., China), followed by electrochemical measurements at each temperature. The process consisted of purging the system with various gases, including pure Ar, pure air, an Ar-H_2 mixture, an H_2-N_2 mixture, and an N_2-O_2 mixture. All gases (including the component gases in the mixtures) were of high purity (≥ 99.999%) and supplied by Dalian Special Gases Co., Ltd., China. The impedance was measured over a frequency range of 7 MHz to 0.1 Hz with an applied voltage of 100 mV. The obtained impedance data were fitted using Zview 3.1 software. The thermogravimetry (TG) curve was recorded on a thermogravimetric analyzer (STA 449 F3,

NETZSCH-Gerätebau GmbH, Germany) over a temperature range of 80 to 1000 ℃. The gas flow rate was set at 20 mL/min, and the heating rate was set at 10 ℃/min. High-purity Ar or air gas (≥ 99.999%, Dalian Special Gases Co., Ltd., China) was used during the measurement. X-Ray Photoelectron Spectroscopy (XPS) characterization was performed using an X-ray photoelectron spectrometer (Axis Supra+, Shimadzu, China) to analyze the chemical state of elements in the samples. The Al/Ag double anode X-ray source was used for excitation. The main peak of C1s at 284.8 eV was used as the reference for charge correction, and the spectra were analyzed using Avantage software. Electron paramagnetic resonance (EPR) spectra were recorded at room temperature using a spectrometer (E500, Bruker Corporation, Germany) operating in the X-band at a frequency of 9.42 GHz.

RESULTS AND DISCUSSION

Structural and morphological characterization

After the first sintering at 1350 °C, the room-temperature XRD pattern of $Ca_{1.46}Ti_{1.38}Nb_{1.11}O_7$ confirmed the formation of the target phase, along with a small amount of TiO_2 as an impurity. This suggests that sintering temperatures below 1350 °C may result in higher impurity levels due to incomplete reaction. To eliminate the TiO_2 impurity and achieve densification, the material was subjected to a second sintering at 1350 °C for 8 h. **Figure 1** shows the refined XRD pattern obtained at 700 ℃ of $Ca_{1.46}Ti_{1.38}Nb_{1.11}O_7$ after the second sintering at 1350 °C. All diffraction peaks can be indexed to the pyrochlore structure**,** indicating the formation of a pure phase. **Table 1** lists the refined structural parameters obtained from in situ XRD data. Because the data were collected at 700 °C, they provide a more realistic representation of the crystal structure at high temperatures, which is essential for accurately predicting the ionic conduction mechanism under operating conditions. $Ca_{1.46}Ti_{1.38}Nb_{1.11}O_7$ is a typical pyrochlore structure with a space group of *Fd-3m* (No. 227, origin choice 2). There are two different kinds of oxygen sites, O1 (48*f*) and O2 (32*e*). The O2 site contains a high concentration of oxygen vacancies, while the O1 site exhibits a relatively low vacancy concentration. These parameters were then used to predict the influence of structural changes on the material's properties. The occupancies of Ca, Ti, and Nb were determined based on the stoichiometry of starting materials. The R_F is below 7%, and R_{wp} and R_p are below 4%, indicating that the refined crystal structure is in excellent agreement with the experimental data[16]. XRF analysis was conducted

to verify the elemental composition of the synthesized material. Quantification was performed using a standardless fundamental parameters (FP) method. The measured oxide contents are 24.5 wt% CaO, 32.3 wt% TiO_2, and 43.2 wt% Nb_2O_5. Based on these values, the calculated molar ratios of Ca, Ti, Nb and O are 1.46:1.35:1.09:6.88, which are very close to the nominal stoichiometry. As shown in **Figure 2**, the EDS mapping diagrams of Ca, Ti, Nb, O confirm that the elements distribute homogeneously without any apparent clustering or segregation[31]. Combined with the XRD results, this confirms the formation of a single-phase $Ca_{1.46}Ti_{1.38}Nb_{1.11}O_7$. **Figure 3A** shows the cross-section SEM image of the $Ca_{1.46}Ti_{1.38}Nb_{1.11}O_7$ pellet. A relatively dense microstructure can be observed, with particle sizes visually estimated to be in the range of several hundred nm. The particles are needle-like in shape. The relative density of the sample reached 92.6% as measured by the Archimedes method, which is close to the upper limit typically achieved by conventional solid-state sintering (manual grinding, uniaxial pressing). This indicates that a sintering temperature of 1350 °C is sufficient for $Ca_{1.46}Ti_{1.38}Nb_{1.11}O_7$ and that higher temperatures are unnecessary. However, the particle size distribution appears inhomogeneous in the SEM image. This observation is consistent with the particle size distribution measured by the laser diffraction particle size analyzer, which gives an average particle size of approximately 412.8 nm with a PDI of 0.371 [**Figure 3B**], confirming a broad size distribution. The inhomogeneity in particle size can be attributed to non-uniform temperature distribution within the pellet during sintering.

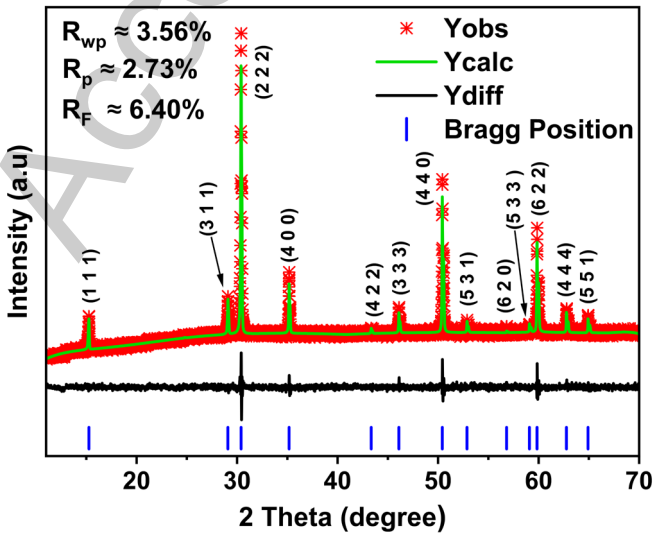

Figure 1. Refined XRD pattern of $Ca_{1.46}Ti_{1.38}Nb_{1.11}O_7$ obtained at 700 °C.

Table 1. The final refined structural parameters for the sample $Ca_{1.46}Ti_{1.38}Nb_{1.11}O_7$ from XRD data at 700 °C: $a = b = c = 10.302$ Å

Atoms	Site	*x*	*y*	*z*	*Occupancy*	*U* (Å²)					
Nb	16*c*	0.0000	0.0000	0.0000	0.5550	0.0124					
Ti1	16*c*	0.0000	0.0000	0.0000	0.4450	0.0129					
Ca	16*d*	0.5000	0.5000	0.5000	0.7300	0.0160					
Ti2	96*g*	0.4681	0.4681	0.5595	0.0408	0.0059					
						U_{11} (Å²)	U_{22} (Å²)	U_{33} (Å²)	U_{12} (Å²)	U_{13} (Å²)	U_{23} (Å²)
O1	48*f*	0.3229	0.1250	0.1250	0.9774	0.0720	0.0020	0.0020	0.0000	0.0000	0.0010
O2	32*e*	0.4013	0.4013	0.4013	0.2254	0.0250	0.0250	0.0250	0.0097	0.0097	0.0097

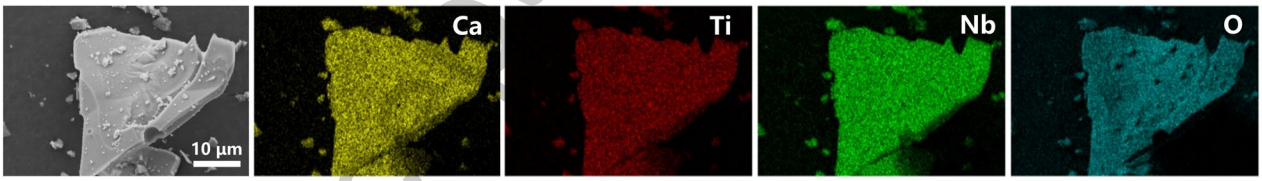

Figure 2. SEM image and corresponding elemental distribution maps of $Ca_{1.46}Ti_{1.38}Nb_{1.11}O_7$ powder.

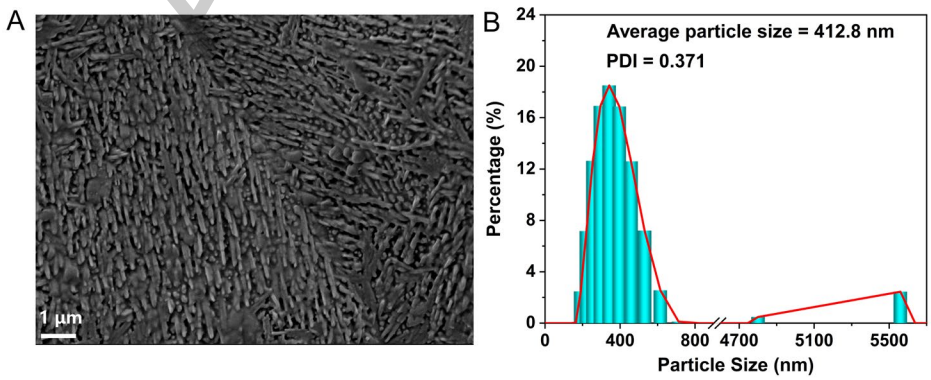

Figure 3. (A) Cross-sectional SEM image of the $Ca_{1.46}Ti_{1.38}Nb_{1.11}O_7$ pellet; (B)

Particle size distribution of $Ca_{1.46}Ti_{1.38}Nb_{1.11}O_7$ measured by laser diffraction.

Electrical properties

Conductivity measurements were first performed in Ar to both prevent oxidation of the material and to assess its electrical response following sintering in Ar. Electrochemical impedance spectroscopy was used to characterize the electrical properties of $Ca_{1.46}Ti_{1.38}Nb_{1.11}O_7$. The resistance in the high frequency range represents the grain resistance, the resistance in the mid-frequency range corresponds to the grain-boundary resistance, and the resistance in the low-frequency range can be due to the polarization effect of the electrodes. The impedance plots [**Figure 4A-C**] exhibit a single, nearly symmetric semicircular arc, which arises from overlapping grain and grain-boundary responses and can be modeled using an equivalent circuit with a single RC (resistance-capacitance) element. The total conductivity (σ_{b+gb}, representing the sum of bulk and grain-boundary contributions) of $Ca_{1.46}Ti_{1.38}Nb_{1.11}O_7$ is presented in the Arrhenius plot in **Figure 4D**. These values were derived from the impedance spectra measured in Ar, 5% H_2/Ar, and air atmospheres over the temperature range of 500-900 ℃. The conductivity (σ) was calculated from the resistance using Equation (1)[32],

$$\sigma = \frac{1}{R} \times \frac{l}{A} \tag{1}$$

where R, l, and A represent the resistance, the spacing between the probes, and the cross-sectional area of the sample, respectively.

σ_{b+gb} of $Ca_{1.46}Ti_{1.38}Nb_{1.11}O_7$ increases gradually with increasing temperature from 500 ℃ to 900 ℃, indicating a thermally activated ionic diffusion process. The conductivity of the sample varies approximately linearly with temperature in air. The temperature dependence of the conductivity in air can be described by Equation (2)[33],

$$\sigma T = \sigma_0 e^{-\frac{E}{k_B T}} \tag{2}$$

where σ, T, σ_0, E, and k_B are the conductivity, absolute temperature, pre-exponential factor, activation energy, and Boltzmann constant, respectively.

Across the entire temperature range, the conductivity follows the order: 5% H_2/Ar >Ar >air, indicating that the material exhibits n-type conduction. The conductivity of $Ca_{1.46}Ti_{1.38}Nb_{1.11}O_7$ was 4.20×10^{-2} S cm^{-1} in 5% H_2/Ar, 9.22×10^{-3} S cm^{-1} in Ar and 2.92×10^{-5} S cm^{-1} in air at 900 °C. **Figure 5** demonstrates that the change in conductivity upon gas switching is reversible. This sensitive and reversible conductivity response to different atmospheres suggests that the material is a promising candidate for gas sensor applications. The DC conductivity σ_{DC} of $Ca_{1.46}Ti_{1.38}Nb_{1.11}O_7$ as a function of oxygen partial pressure (pO_2) is shown in **Figure 6A**. At 900 °C, σ_{DC} decreases with increasing pO_2, which is consistent with n-type conduction. σ_{DC} changes little with the oxygen partial pressure in the range of 1.0×10^{-5} to 1.0 atm at 500 °C, indicating that the conductivity is primarily ionic at this temperature. Negligible proton conduction is observed because there is little difference in σ_{DC} of $Ca_{1.46}Ti_{1.38}Nb_{1.11}O_7$ under wet and dry air flows [**Figure 6B**]. Electromotive force (EMF) measurements were conducted to determine the ion transport number (t_{ion}) of the material under different atmospheres [**Figure 7**]. Using an air | N_2 gas concentration cell, the t_{ion} value is 0.995 at 500 °C, indicating that the material is an almost pure oxide-ion conductor at this temperature. The t_{ion} values in the entire temperature range are above 0.8, suggesting that oxide-ion conduction is dominant in oxidizing (air, O_2) and inert (Ar, N_2) atmospheres. In contrast, EMF measurements using an air | 5% H_2/N_2 gas concentration cell revealed a drastically different behavior. The t_{ion} values are below 0.25 in the whole temperature range, indicating that the material exhibits predominantly electronic conduction under a reducing atmosphere (e.g., 5% H_2/N_2, 5% H_2/Ar). **Figure 8** presents a comparison of the conductivity of $Ca_{1.46}Ti_{1.38}Nb_{1.11}O_7$ with that of recently reported pyrochlores. Compared with these pyrochlores, the conductivity of $Ca_{1.46}Ti_{1.38}Nb_{1.11}O_7$ is lower in air, comparable in Ar, and significantly higher in 5% H_2/Ar. σ_{DC} remains stable over 27 hours [**Figure 9A**], demonstrating the excellent long-term stability of the material. No significant degradation in σ_{b+gb} is observed over 7 thermal cycles between 100 °C and 900 °C [**Figure 9B**], demonstrating the high structural stability of the material under repeated thermal cycling. These results indicate that $Ca_{1.46}Ti_{1.38}Nb_{1.11}O_7$ is suitable for high-temperature applications.

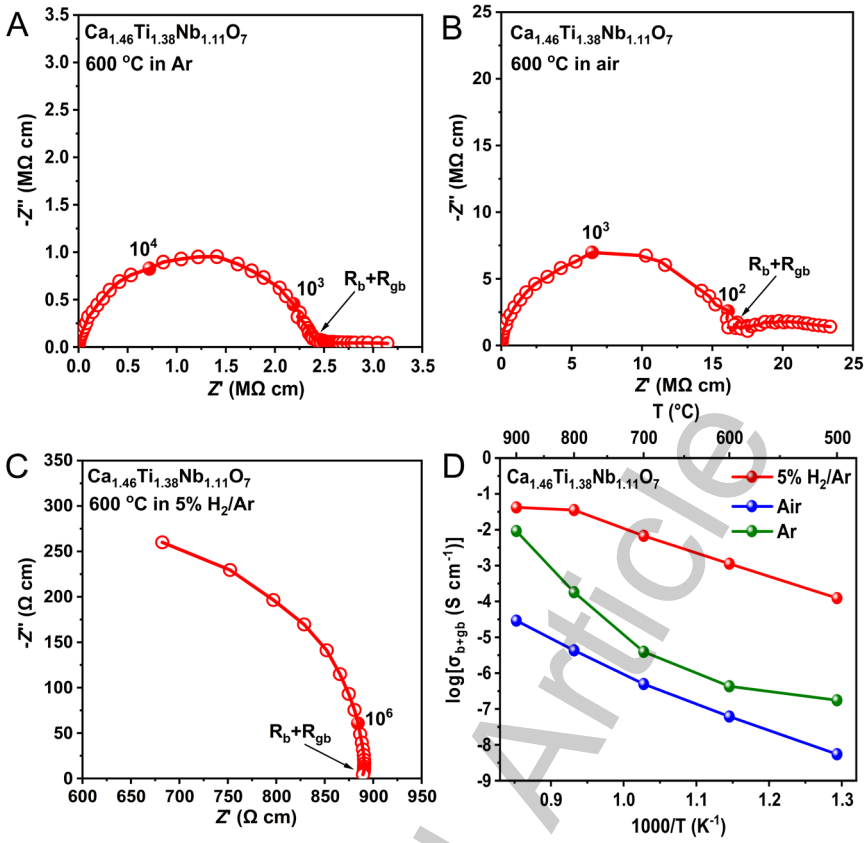

Figure 4. (A) The complex impedance plot obtained at 600 °C in Ar of $Ca_{1.46}Ti_{1.38}Nb_{1.11}O_7$; (B) The complex impedance plot obtained at 600 °C in air of $Ca_{1.46}Ti_{1.38}Nb_{1.11}O_7$; (C) The complex impedance plot obtained at 600 °C in 5% H_2/Ar of $Ca_{1.46}Ti_{1.38}Nb_{1.11}O_7$; (D) The total conductivity σ_{b+gb} of $Ca_{1.46}Ti_{1.38}Nb_{1.11}O_7$ in the range of 500-900 °C in 5% H_2/Ar, Ar, and air (data from impedance curve fitting).

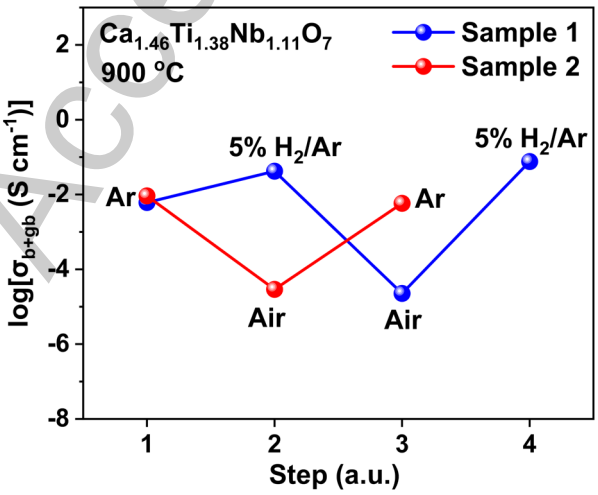

Figure 5. Reversibility of the conductivity of $Ca_{1.46}Ti_{1.38}Nb_{1.11}O_7$ upon switching between 5% H_2/Ar, air and Ar at 900 °C.

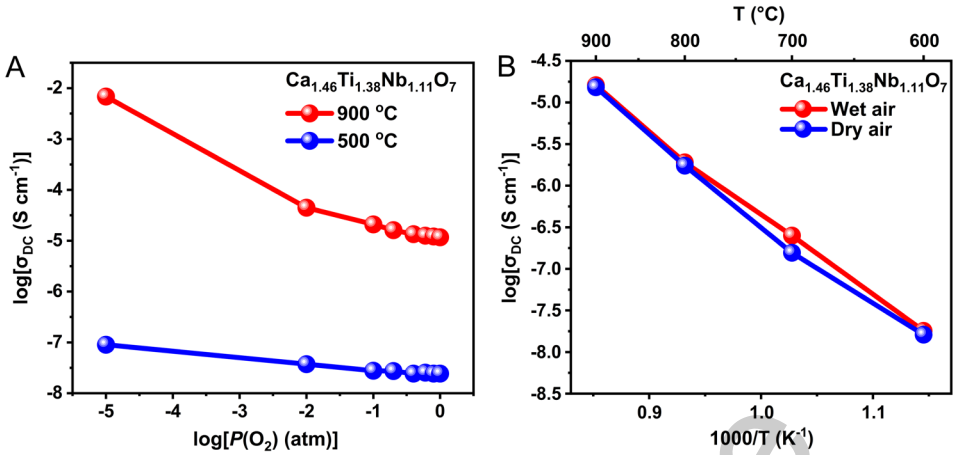

Figure 6. (A) Oxygen partial pressure pO_2 dependence of the DC conductivity σ_{DC} of $Ca_{1.46}Ti_{1.38}Nb_{1.11}O_7$ at 500 °C and 900 °C; (B) Arrhenius plots of σ_{DC} of $Ca_{1.46}Ti_{1.38}Nb_{1.11}O_7$ in wet (water vapor pressure of 0.042 atm) and dry air.

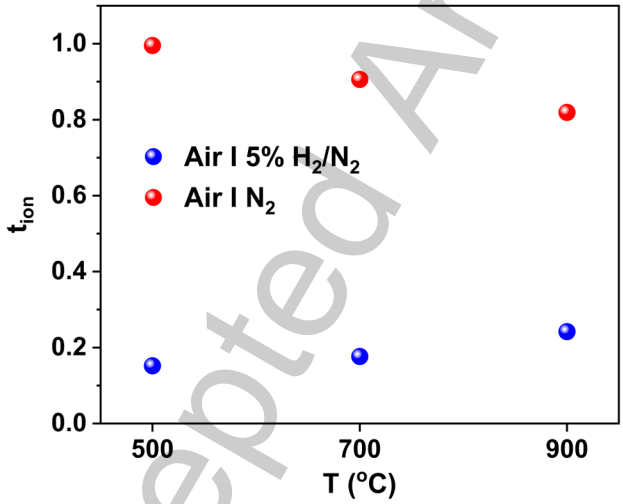

Figure 7. Ion transport number t_{ion} of $Ca_{1.46}Ti_{1.38}Nb_{1.11}O_7$ from EMF measurements using air | N_2 and air | 5% H_2/N_2 gas concentration cells.

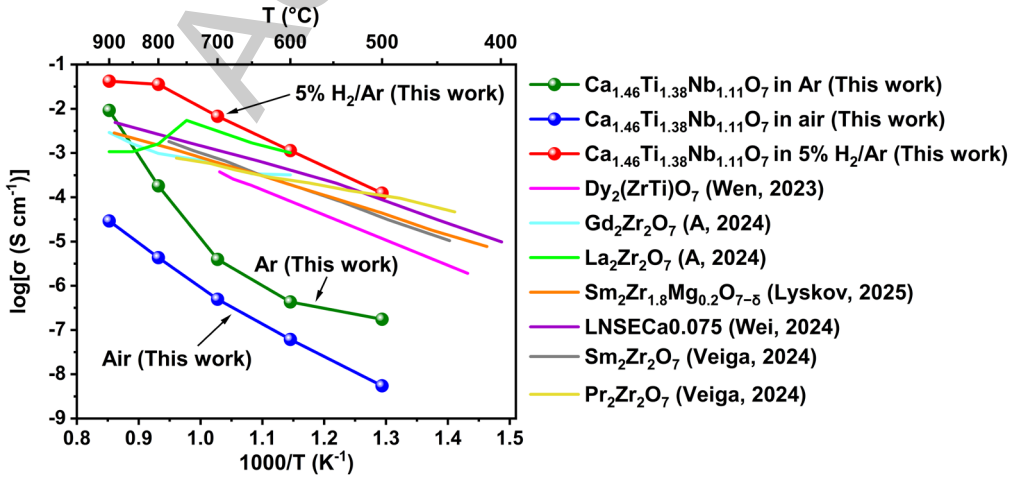

Figure 8. Comparison of the conductivity of $Ca_{1.46}Ti_{1.38}Nb_{1.11}O_7$ with that of recently reported pyrochlores[11, 14, 16, 34, 35].

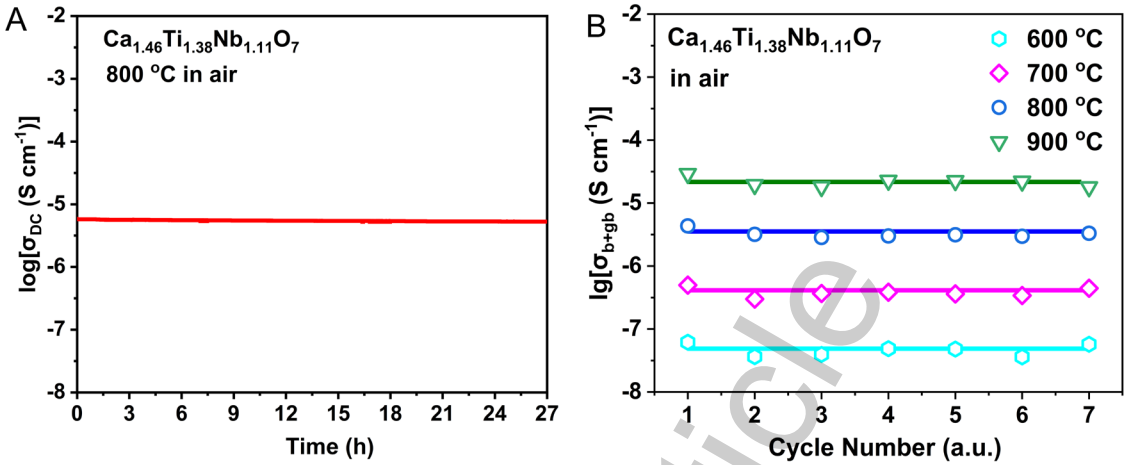

Figure 9. (A) Time dependence of the DC conductivity σ_{DC} of $Ca_{1.46}Ti_{1.38}Nb_{1.11}O_7$ at 800 °C in air; (B) The total conductivity σ_{b+gb} in air of $Ca_{1.46}Ti_{1.38}Nb_{1.11}O_7$ from 600 to 900 °C during the thermal cycling process between 100 °C and 900 °C.

Conduction mechanism

Thermogravimetry

The TG curve of $Ca_{1.46}Ti_{1.38}Nb_{1.11}O_7$ in air [**Figure 10**] showed an overall mass gain with increasing temperature, reaching 101.13% of the initial mass up to 1000 °C. The mass gain is attributed to the addition of oxygen atoms in the air into the lattice. The incorporation of oxygen atoms decreases the oxygen vacancy concentration, thereby reducing the conductivity. $Ca_{1.46}Ti_{1.38}Nb_{1.11}O_7$ exhibited negligible mass change upon heating in Ar [**Figure 10**], owing to the extremely low oxygen partial pressure. It can be inferred from the TG curve in Ar that no significant change in oxygen vacancy concentration occurred during the conductivity measurements from 500 to 900 °C in Ar. Therefore, the oxygen vacancy concentration in the material is significantly higher during conductivity measurement in Ar than in air, leading to a notably higher conductivity in Ar.

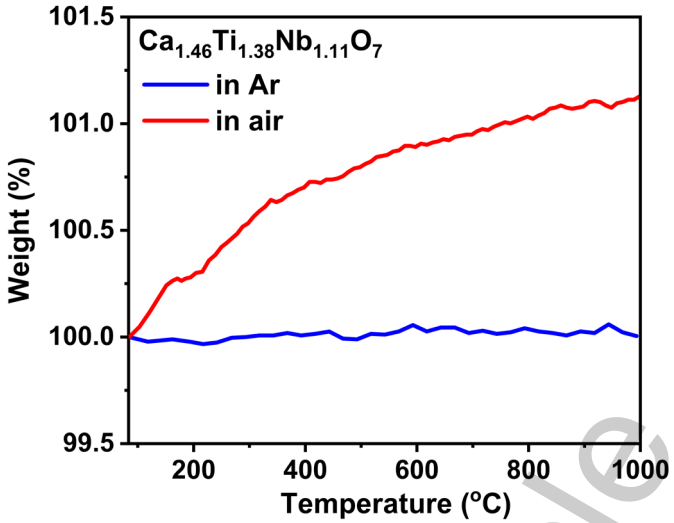

Figure 10. The TG curve of $Ca_{1.46}Ti_{1.38}Nb_{1.11}O_7$ in air and Ar.

X-ray photoelectron spectroscopy

To directly compare the oxygen vacancy concentrations in $Ca_{1.46}Ti_{1.38}Nb_{1.11}O_7$ under different atmospheres, the Ar-synthesized sample was subjected to annealing under contrasting atmospheres (in air and H_2). The samples before and after annealing treatment were then characterized by XPS for comparison. The wide-survey XPS spectra [**Figure 11**] show all characteristic peaks of $Ca_{1.46}Ti_{1.38}Nb_{1.11}O_7$. The core-level peaks observed at 530.0, 458.1, 346.9, and 207.1 eV correspond to O 1s, Ti 2p, Ca 2p, and Nb 3d, respectively, confirming the presence of these elements. No other elements were observed in the wide-survey spectra, indicating that no impurities were incorporated during the preparation process. The Ca 2p spectra [**Figure 12A**] show prominent peaks at 346.7 eV and 350.2 eV, corresponding to the Ca 2p3/2 and Ca 2p1/2 peaks, respectively[36]. The spin-orbit splitting is 3.5 eV, and the chemical valence is +2. The Ti 2p spectra of both the pristine and the air-annealed samples [**Figure 12B**] exhibited prominent peaks at 458.4 eV and 464.3 eV, corresponding to the Ti 2p3/2 and Ti 2p1/2 peaks, respectively[37]. A spin-orbit splitting of 5.9 eV was observed, common to both samples, corresponding to Ti^{4+}. In the Ti 2p spectrum of the H_2-annealed sample [**Figure 12B**], the peaks observed at 456.6 eV and 462.8 eV are assigned to the Ti^{3+} 2p3/2 and Ti^{3+} 2p1/2, respectively[38-40]. During H_2-annealing of $Ca_{1.46}Ti_{1.38}Nb_{1.11}O_7$, electron injection into the conduction band results in the partial reduction of Ti^{4+} to Ti^{3+}, which contributes to the material's high conductivity in 5% H_2/Ar[41]. This is consistent with EMF measurements under an air | 5% H_2/N_2 gas concentration cell, which revealed that the t_{ion} values are below 0.25 across the entire

temperature range, confirming predominantly electronic conduction under a reducing atmosphere [**Figure 7**]. The Nb 3d spectra [**Figure 12C**] show prominent peaks at 206.8 eV and 209.7 eV, corresponding to the Nb 3d5/2 and Nb 3d3/2 peaks, respectively[42]. The spin-orbit splitting is 2.9 eV, and the chemical valence is +5. In the O 1s spectra [**Figure 12D**], the peaks near 529.7 eV represent metal-oxygen bonds (Ca-O, Ti-O, Nb-O), while the peaks near 531.6 eV represent oxygen vacancies[43-48]. The spectral asymmetry suggests variations in metal-oxygen bonding and the presence of oxygen vacancies in the lattice. The corresponding computed percentage of oxygen vacancies is 45.2% before air-annealing and 31.7% after air-annealing[11]. The higher percentage of oxygen vacancies leads to the higher conductivity, while oxygen vacancies provide better channels for oxide-ion conduction[49]. After the Ar-synthesized sample was air-annealed, it exhibited a reduction in oxygen vacancy concentration and corresponding low conductivity. Following H_2-annealing, the lattice oxygen content in $Ca_{1.46}Ti_{1.38}Nb_{1.11}O_7$ was further reduced to 34.48%, as H_2 removed lattice oxygen in the form of water vapor. This led to the formation of oxygen vacancies, which are largely occupied by adsorbed oxygen species. The reduction process was facilitated by electron injection into the conduction band, weakening metal-oxygen bonds and promoting oxygen loss[41]. The reversibility of the conductivity change upon atmosphere switching suggests that the changes of oxygen vacancies are also reversible [**Figure 5**].

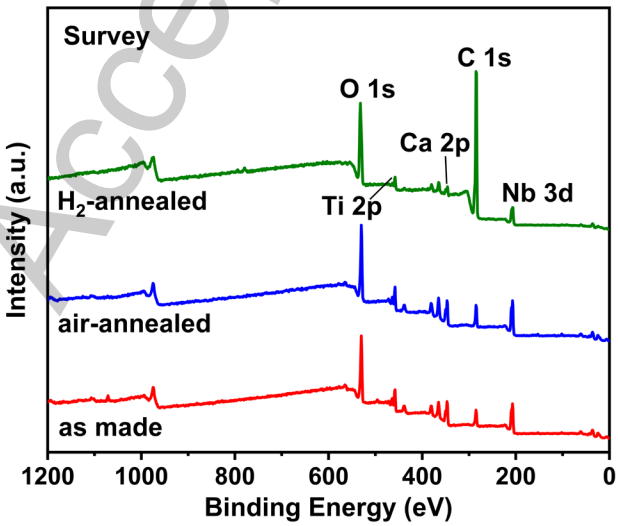

Figure 11. Wide XPS survey spectra of $Ca_{1.46}Ti_{1.38}Nb_{1.11}O_7$.

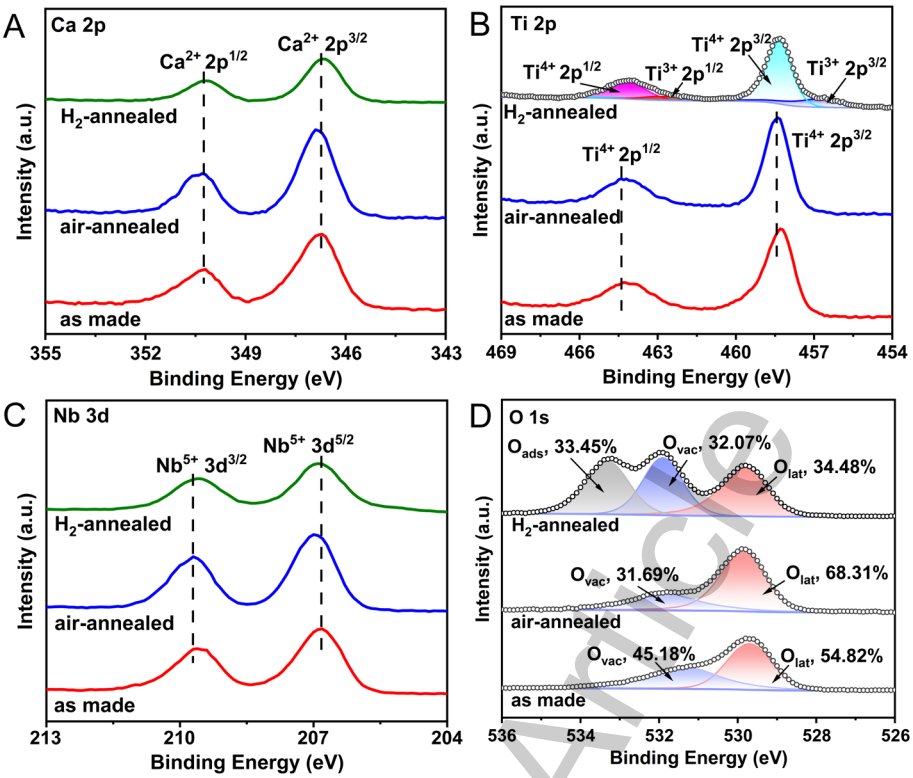

Figure 12. XPS spectra of $Ca_{1.46}Ti_{1.38}Nb_{1.11}O_7$. (A) Ca 2p spectra; (B) Ti 2p spectra; (C) Nb 3d spectra; (D) O 1s spectra.

Electron paramagnetic resonance

Although sintering in Ar generated a large number of oxygen vacancies in $Ca_{1.46}Ti_{1.38}Nb_{1.11}O_7$, the valence states of the metal elements remained unchanged. This phenomenon, where oxygen vacancies form without reduction of the metal cations, was also observed in R-WO_3 by Ning Zhang et al[43]. While the charge-compensating electrons from oxygen vacancies can be either trapped by metal ions or localized at the vacancy sites, $Ca_{1.46}Ti_{1.38}Nb_{1.11}O_7$ is an example of the latter[41]. The EPR spectrum [**Figure 13**] shows a symmetric signal at g = 2.0014, which is consistent with electrons being trapped at oxygen vacancies[43, 50-56]. The weak intensity of the EPR signal indicates a very small number of unpaired electrons, suggesting a relatively minor contribution of electronic conduction in $Ca_{1.46}Ti_{1.38}Nb_{1.11}O_7$. This is supported by preceding EMF measurements under an air | N_2 gas concentration cell, which revealed that the t_{ion} values are above 0.8 across the entire temperature range [**Figure 7**]. When heating $Ca_{1.46}Ti_{1.38}Nb_{1.11}O_7$ in Ar, the generation of oxygen vacancies can be described by Equation (3)[41],

$$O_O^x \rightleftharpoons V_{\ddot{O}} + 2e^- + \frac{1}{2}O_2 \quad (3)$$

where O_O^x represents a neutral lattice oxygen atom, $V_{\ddot{O}}$ represents an oxygen vacancy in the +2 charge state, and e^- represents electrons.

Accordingly, the equilibrium $V_{\ddot{O}}$ concentration, $[V_{\ddot{O}}]$, can be described by Equation (4)[41],

$$K = [V_o^{\cdot\cdot}] \cdot p_{O_2}^{1/2} / [O_o^x] = \exp\left(\frac{-\Delta G_f}{k_b T}\right) \quad (4)$$

where K is the equilibrium constant, k_B is the Boltzmann constant, pO_2 is the O_2 partial pressure, ΔG_f is the formation free energy of $V_{\ddot{O}}$, and $[O_O^x]$ is the lattice oxygen concentration.

Based on Equation (4), a decrease in pO_2 leads to an increase in $[V_{\ddot{O}}]$. This provides a rationale for creating oxygen vacancies in a low-oxygen atmosphere or under vacuum.

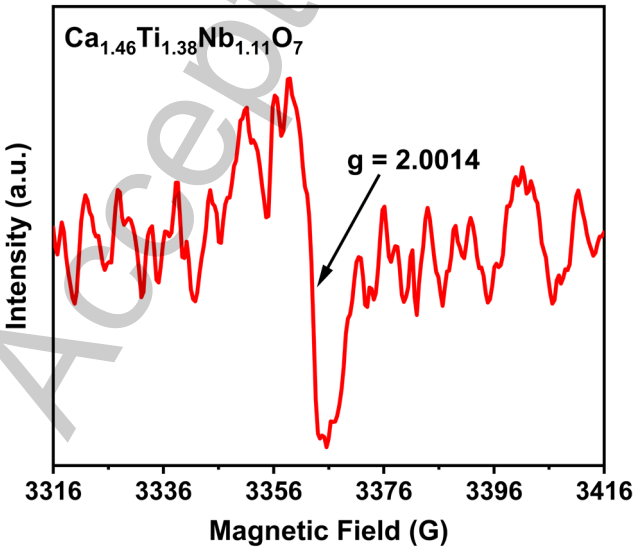

Figure 13. EPR spectrum at room-temperature of $Ca_{1.46}Ti_{1.38}Nb_{1.11}O_7$.

Bond valence site energy calculations and maximum entropy method

Studying the oxide-ion migration pathways is crucial for understanding the electrochemical behavior of the material. BVSE calculations, based on Pauling's

principle of local charge neutrality, were performed by placing the mobile ion at all points of a three-dimensional grid that spans the unit cell[57]. This grid represents a fixed, rigid structural framework. The BVSE method has been extensively used to identify crystalline frameworks with infinite networks that facilitate the transport of ions. It also serves to rank materials based on the accessible volume within the crystal structure where the valence mismatch is low. The migration pathways are simulated through a two-step process: first, transition positions between equilibrium sites are identified by calculating the ion's valence state; then, the complete pathways are reconstructed by connecting these positions. The oxide-ion migration pathways in $Ca_{1.46}Ti_{1.38}Nb_{1.11}O_7$ were simulated by BVSE calculations. At an iso-surface value (oxide-ion migration barrier) of 0.55 eV, the O1-site atoms are interconnected [**Figure 14A**]. Simultaneously, O1 and O2 sites are connected. This indicates that oxide ion migration occurs through O1–O1 and O2–O1–O2 pathways within the lattice, confirming three-dimensional oxide-ion diffusion. The results highlight the importance of O1-site vacancies for oxide-ion migration, as O2-site atoms must pass through the O1 site during migration. Thus, creating oxygen vacancies at the O1 site will enhance the conductivity of O2-site atoms. The MEM electron density distribution of oxide ions along the migration pathway exhibits good agreement with the BVSE calculations [**Figure 14B**], thereby further confirming the reliability of the BVSE results. Notably, the oxide-ion migration barrier calculated in this work (0.55 eV) is lower than that derived from the crystal structure reported by R.S. Roth et al.[27] (1.14 eV). This difference can be attributed primarily to the different conditions under which the XRD data were obtained. The structure reported by Roth et al. was determined from room-temperature XRD data, whereas our calculations are based on crystal structure parameters refined from high-temperature XRD data. Oxide-ion conduction is a thermally activated process. Therefore, the high-temperature structure provides a more accurate representation of the conduction behavior. This structure more accurately captures the migration pathways and local coordination environments under operating conditions, thereby providing a more reliable basis for the calculated migration barrier. The reliability of our refined result is further supported by the high quality of the Rietveld refinement, with $R_F < 7\%$ and both R_{wp} and $R_p < 4\%$. These low residual factors ensure the accuracy of the refined crystal structure and further guarantee the credibility of the subsequent BVSE calculations. Therefore, the

calculation results in this work represent the high-temperature conduction behavior of $Ca_{1.46}Ti_{1.38}Nb_{1.11}O_7$ more realistically.

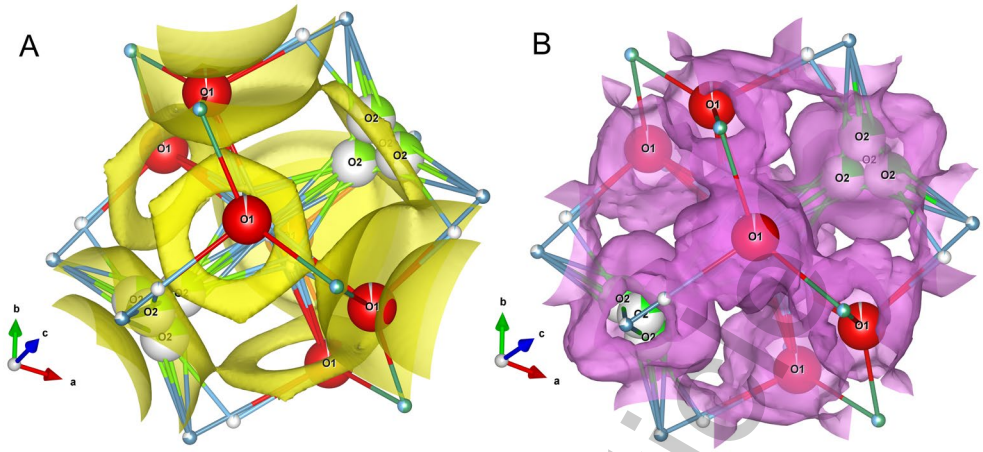

Figure 14. BVSE and MEM calculations for $Ca_{1.46}Ti_{1.38}Nb_{1.11}O_7$. (A) The calculated BVSE map of oxide ions with an iso-surface at 0.55 eV, where the iso-surface is marked by yellow areas; (B) MEM electron density distribution for oxide ions, where the electron density is marked by pink areas.

CONCLUSIONS

This work aims to investigate the conductive properties and conduction mechanism of $Ca_{1.46}Ti_{1.38}Nb_{1.11}O_7$. The conductivity of $Ca_{1.46}Ti_{1.38}Nb_{1.11}O_7$ is strongly dependent on the oxygen partial pressure, exhibiting significantly enhanced conductivity under a reducing atmosphere. The variations in conductivity across different atmospheres can be attributed to changes in the oxygen vacancy concentration and the valence states of the metal cations. These results confirm that creating oxygen vacancies through synthesis in a low-oxygen atmosphere is an effective strategy for enhancing ionic conductivity. Future research will focus on optimizing the defect chemistry by carefully controlling the synthesis atmosphere to further enhance the material's performance.

DECLARATIONS

Authors' contributions

Yuan Yao: Methodology, Data curation, Investigation, Writing - original draft.

Shuhang Liu: Methodology, Investigation.

Heyuan Sun: Methodology, Investigation.

Jiajia Yao: Methodology, Investigation.

Wen-Cui Li: Funding acquisition, Investigation, Methodology, Supervision.

Wenrui Zhang: Data curation, Funding acquisition, Investigation, Methodology, Supervision, Writing - original draft, Writing – review & editing.

Availability of data and materials

The original contributions presented in this study are included in the article. Further inquiries can be directed to the corresponding author.

AI and AI-assisted tools statement

Not applicable.

Financial support and sponsorship

This work was financially supported by National Natural Science Foundation of China (NSFC) (No. 22478066) and Fundamental Research Funds for the Central Universities, DUT23RC(3)024.

Conflicts of interest

All authors declared that there are no conflicts of interest.

Ethical approval and consent to participate

Not applicable.

Consent for publication

Not applicable.

REFERENCES

1. Yu, H.; Ma, M.; Su, Y.; Dong, D.; Hu, X.; Wei, T. Environmentally regulated intrinsic oxygen-ion transport for oxideion conductors. *J. Materiomics.* **2023**, 9, 867-873. DOI: 10.1016/j.jmat.2023.02.009

2. Ueno, N.; Yaguchi, H.; Fujii, K.; Yashima, M. High conductivity and diffusion

mechanism of oxide ions in triple fluorite-like layers of oxyhalides. *J. Am. Chem. Soc.* **2024**,.146, 11235-11244. DOI: 10.1021/jacs.4c00265

3. Kreysa, G.; Qta, K.; Savinell, R. F. *Encyclopedia of Applied Electrochemistry*, Springer, 2014. DOI: 10.1007/978-1-4419-6996-5.

4. Zhang, W.; Fujii, K.; Ishiyama, T.; Kandabashi, H.; Yashima, M. Dion–Jacobson-type oxide-ion conductor $CsLa_2Ti_2NbO_{10-\delta}$ without phase transitions, *J. Mater. Chem. A*, **2020**, 8, 25085-25093. DOI: 10.1039/D0TA06135B

5. Zhang, W.; Fujii, K.; Niwa, E.; et al. Oxide-ion conduction in the Dion-Jacobson phase $CsBi_2Ti_2NbO_{10-\delta}$. *Nat. Commun.* **2020**, 11, 1224-1231. DOI: 10.1038/s41467-020-15043-z

6. Wang, H.; Ma, Y.; Yang, W.; et al. Understanding the conduction mechanism of acceptor-doped ceria oxygen ion conductors by photoluminescence analysis. *Ceram. Int.* **2022**, 48, 27343-27348. DOI: 10.1016/j.ceramint.2022.05.119

7. Li, X.; Yang, L.; Zhu, Z.; Wang, X.; Chen, P.; Huang, S.; Wei, X.; Cai, G.; Manuel, P.; Yang, S.; Lin, J.; Kuang, X.; Sun, J. Borates as a new direction in the design of oxide ion conductors. *Sci. China Mater.* **2022**, 65, 2737-2745. DOI: 10.1007/s40843-022-2044-3

8. Dunn, B.; Kamath, H.; Tarascon, J. Electrical energy storage for the grid: A battery of choices. *Science* **2011**, 334, 928-935. DOI: 10.1126/science.1212741

9. Kharton, V.; Marques, F.; Atkinson, A. Transport properties of solid oxide electrolyte ceramics: a brief review. *Solid State Ion* **2004**, 174, 135-149. DOI: 10.1016/j.ssi.2004.06.015

10. Kudo, T.; Obayashi, H. Oxygen ion conduction of the fluorite-type $Ce_{1-x}Ln_xO_{2-x/2}$ (Ln = lanthanoid element) . *J. Electrochem. Soc.* **1975**, 122, 142-147. DOI: 10.1149/1.2134143

11. Raj, A. A.; Anantharaman, A. P. Exploring the defect formation and ionic migration in $A_2Zr_2O_7$ (A = La, Ce, Nd, and Gd) Pyrochlore solid-state electrolytes. *Ceram. Int.* **2024**, 50, 48116-48126. DOI: 10.1016/j.ceramint.2024.09.16

12. Liu, Z.; Ouyang, J.; Sun, K.; Zhou, Y.; Xiang, J. Preparation, structure and electrical conductivity of pyrochlore-type $Gd_{1-x}Eu_{2x}Sm_{1-x}Zr_2O_7$ ceramics with a constant lattice parameter. *Electrochim. Acta* **2011**, 56, 7045-7050. DOI: 10.1016/j.electacta.2011.06.001

13. Cao, X. Q.; Vassen, R.; Jungen, W.; et al. Thermal stability of lanthanum zirconate plasma-sprayed coating. *J. Am. Ceram. Soc.* **2001**, 84, 2086-2090. DOI:

10.1111/j.1151-2916.2001.tb00962.x

14. Understanding the rapid reoxidation process and the electrical properties of Spark Plasma sintered pyrochlores. *J. Eur. Ceram. Soc.* **2024**, 44, 4130-4140. DOI: 10.1016/j.jeurceramsoc.2023.12.070

15. Marrocchelli, D.; Madden, P. A.; Norberg, S. T.; Hull, S. Structural disorder in doped zirconias, Part II: Vacancy ordering effects and the conductivity maximum. *Chem. Mater.* **2011**, 23, 1365-1373. DOI: 10.1021/cm102809t

16. Wen, L. C.; Li, Z. P.; Chen, H. S.; Tseng, S. C. Preparation and electrical properties of pyrochlore $R_2(ZrTi)O_7$ for solid oxide fuel cell electrolyte. *J. Energy Storage* **2023**, 64, 107058-107064. DOI: 10.1016/j.est.2023.107058

17. Subramanian, M. A.; Aravamudan, G.; Subba Rao, G. V. Oxide pyrochlores - A review. *Prog. Solid State Chem.* **1983**, 15, 55-143. DOI: 10.1016/0079-6786(83)90001-8

18. Blundred, G. D.; Bridges, C. A.; Rosseinsky, M. J. New oxidation states and defect chemistry in the pyrochlore structure. *Angew. Chem., Int. Ed.* **2004**, 43, 3562-3565. DOI: 10.1002/anie.200453819

19. Mouta, R.; Silva, R. X.; Paschoal, C. W. A. Tolerance factor for pyrochlores and related structures. *Acta Crystallogr., Sect. B* **2013**, 69, 439-445. DOI: 10.1107/S2052519213020514

20. Mahato, N.; Banerjee, A.; Gupta, A.; Omar, S.; Balani, K. Progress in material selection for solid oxide fuel cell technology: A review. *Prog. Mater. Sci.* **2015**, 72, 141-337. DOI: 10.1016/j.pmatsci.2015.01.00

21. Varcoe, J. R.; Atanassov, P.; Dekel, D. R.; et al. Anion-exchange membranes in electrochemical energy systems. *Energy Environ. Sci.* **2014**, 7, 3135-3191. DOI: 10.1039/C4EE01303D

22. Cioateră, N.; Voinea, E.; Spînu, C. Pyrochlores as cathodes in solid oxide fuel cells. In *Pyrochlore Ceramics*; Chowdhury, A., Ed.; Elsevier, 2022; pp 433–448. DOI: 10.1016/B978-0-323-90483-4.00013-1

23. Shlyakhtina, A. V.; Pigalskiy, K. S. Tolerance factor as the basic criterion in searching for promising oxygen-ion and proton conductors among $Ln_{2-x}D_xM_2O_{7-\delta}$ (Ln = La-Lu; M = Sn, Ti, Zr, Hf; D = Sr, Ca, Mg; x = 0, 0.1) 3+/4+ pyrochlores. *Mater. Res. Bull.* **2019**, 116, 72-78. DOI: 10.1016/j.materresbull.2019.04.021

24. Jiang, L.; Liu, Y.; Sun, W; et al. Mixed potential type sensor based on $Gd_2Zr_2O_7$ solid electrolyte and $BiVO_4$ sensing electrode for effective detection of triethylamine. *J.*

Hazard. Mater. **2022**, 440, 129695-129706. DOI: 10.1016/j.jhazmat.2022.129695

25. Ganesan, M.; Jayaraman, V.; Selvaraj, P.; Mani, K. M.; Kim, D. Pyrochlore cerium stannate ($Ce_2Sn_2O_7$) for highly sensitive NO_2 gas sensing at room temperature. *Appl. Surf. Sci.* **2023**, 624, 157135-157145. DOI: 10.1016/j.apsusc.2023.157135

26. Jiang, L.; Wang, C.; Wang, J.; et al. Pyrochlore Ca-doped $Gd_2Zr_2O_7$ solid state electrolyte type sensor coupled with ZnO sensing electrode for sensitive detection of HCHO. *Sensors and Actuators B: Chemical* **2020**, 309, 127768-127775. DOI: 10.1016/j.snb.2020.12776

27. Rotha, R. S.; Vanderah, T. A.; Bordet, P.; et al. Pyrochlore formation, phase relations, and properties in the CaO - TiO_2-$(Nb,Ta)_2O_5$ systems. *J. Solid State Chem.* **2008**, 181, 406-414. DOI: 10.1016/j.jssc.2007.12.005

28. Chen, H. M.; Wong, L. L.; Adams, S. SoftBV - a software tool for screening the materials genome of inorganic fast ion conductors. *Acta Cryst.* **2019**, 75, 18-33. DOI: 10.1107/S2052520618015718

29. Chen, H. M.; Adams, S. Bond softness sensitive bond-valence parameters for crystal structure plausibility tests. *IUCrJ* **2017**, 4, 614-625. DOI: 10.1107/S2052252517010211

30. Wong, L. L.; Phuah, K. C.; Dai, R.; et al. Bond valence pathway analyzer - An automatic rapid screening tool for fast ion conductors within softBV. *Chem. Mater.* **2021**, 33, 625-641. DOI: 10.1021/acs.chemmater.0c03893

31. Liu, F.; Sun Y., Li, Z.; et al. Equivalent doping of Te leads to optimized electrical and thermal transport properties in thermoelectric $Cu_2MnSnSe_4$ alloys. *Microstructures* **2025**, 5, 2025043-2025054. DOI: 10.20517/microstructures.2024.125

32. Zheng, F.; Qiu, R.; Zhang, J.; Tao, Z.; Lei, L. Theoretical and experimental investigation on using Arrhenius equation to analyze conductivities of proton ceramic electrolytes. *Mater. Sci. Eng.: B* **2025**, 322, 118580-118587. DOI: 10.1016/j.mseb.2025.118580.

33. Liu, Z.-G.; Ouyang, J.-H.; Sun, K.-N. Improvement of Electrical Conductivity of Trivalent Rare-earth Cation-doped Neodymium Zirconate by Co-doping Gadolinium and Ytterbium. *Fuel Cells* **2010** , 10 (6), 1050-1056. DOI: 10.1002/fuce.201000107.

34. Wei, H.; Chen, W.; Hou, K.; Duan, X.; Liu, L.; Xu, J. Phases, Electrical Properties, and Stability of High-Entropy Pyrochlores $[(La_{0.25}Nd_{0.25}Sm_{0.25}Eu_{0.25})_{1-x}Ca_x]_2Zr_2O_{7-\delta}$ Oxides. *Phys. Status Solidi A* **2024**; 221:2300753-2300761. DOI: 10.1002/pssa.202300753

35. Lyskov, N. V.; Kolbanev, I. V.; Borunova, A. B.; Vorobieva, G. A.; Abrantes, J. C. C.; Gomes, E.; Danilov, N. A.; Medvedev, D. A.; Shlyakhtina, A. V. Study of Mg doping on the zirconium and lanthanide sites of $Ln_2Zr_2O_7$ (Ln = Sm, Gd) pyrochlores. *Ceram. Int*. **2025** ,51, 32808–32820. DOI: 10.1016/j.ceramint.2025.05.015

36. Batis, N. H.; Delichere, P.; Batis, H. Physicochemical and catalytic properties in methane combustion of $La_{1-x}Ca_xMnO_{3\pm y}$ ($0\leq X\leq 1$; $-0.04\leq y\leq 0.24$). *Appl. Catal. A-Gen.* **2005**, 282, 173-180. DOI: 10.1016/j.apcata.2004.12.009

37. Shi, Y. J.; Zhang, Z.; Dai, Y. Z.; Li, J. X.; Chen, Z. Y. Influence of current density on the photocatalytic activity of Nd:TiO_2 coatings. *J. Wuhan. Univ. Technol. Mater. Sci. Ed.* **2024**, 39, 32-38. DOI: 10.1007/s11595-024-2851-4

38. Dwivedi, C.; Mohammad, T.; Kumar, V.; Dutta, V. Ti^{3+} and oxygen defects controlled colored TiO_2 nanoparticles by continuous spray pyrolysis. *Vacuum* **2020**, 182, 109612-109619. DOI: 10.1016/j.vacuum.2020.109612

39. Wen, P.; Zhang, Y.; Xu, G.; et al. Ti^{3+} self-doped TiO_2 as a photocatalyst for cyclohexane oxidation under visible light irradiation. *J. Materiomics* **2019**, 5, 696-701. DOI: 10.1016/j.jmat.2019.04.009

40. XPS study of cobalt doped TiO_2 films prepared by pulsed laser deposition. *Surf. Interface Anal.* **2014**, 46, 1043-1046. DOI: 10.1002/sia.5397

41. Wang, Z.; Lin, R.; Huo, Y.; Li, H.; Wang, L. Formation, detection, and function of oxygen vacancy in metal oxides for solar energy conversion. *Adv. Funct. Mater.* **2022**, 32, 2109503-2109517. DOI: 10.1002/adfm.202109503

42. Kuneva, M. K.; Krastev, V. I. XPS - investigation of proton exchanged waveguides in $LiNbO_3$. *J. Mater. Sci-Mater. Electron.* **2000**, 11, 629-32. DOI: 10.1023/A:1008988915099

43. Zhang, N.; Li, X.; Ye, H.; et al. Oxide defect engineering enables to couple solar energy into oxygen activation. *J. Am. Chem. Soc.* **2016**, 138, 8928-35. DOI: 10.1021/jacs.6b04629

44. Sun, Q.; Yi, Q.; Luo, H.; Liu, Q.; Zhang, D. Improved piezo-photocatalytic activity by controlling the oxygen vacancy content of $NaNbO_3$ powders. *J. Alloys Compd*. **2025**, 1010, 177687-177695. DOI: 10.1016/j.jallcom.2024.177687.

45. Easton, C. D.; Morgan, D. J. Critical examination of the use of x-ray photoelectron spectroscopy (XPS) O 1s to characterize oxygen vacancies in catalytic materials and beyond. *J. Vac. Sci. & Technol. A* **2025**, 43 (5), 053205-053223. DOI: 10.1116/6.0004686.

46. Wang, J.; Mueller, D. N.; Crumlin, E. J. Recommended strategies for quantifying oxygen vacancies with X-ray photoelectron spectroscopy. *J. Eur. Ceram. Soc*. **2024**, 44, 116709-116716. DOI: 10.1016/j.jeurceramsoc.2024.116709.

47. Raj, A. K. V.; Banerjee, R. H.; Sanwal, J.; Pathak, N.; Chaudhary, N.; Arya, A.; Sengupta, P. Ordering of oxygen vacancies in hydroxyapatite under electron irradiation. *Mater. Chem. Phys.* **2024**, 322, 129609-129620. DOI: 10.1016/j.matchemphys.2024.129609.

48. Zhang, M.; Duan, X.; Gao, Y.; Zhang, S.; Lu, X.; Luo, K.; Ye, J.; Wang, X.; Niu, Q.; Zhang, P.; Dai, S. Tuning Oxygen Vacancies in Oxides by Configurational Entropy. *ACS Appl. Mater. & Interfaces* **2023** ,15, 45774-45789. DOI: 10.1021/acsami.3c07268

49. Li, C.; Zhou, Z.; Lou, Y.; Fu, L. Lattice softening in thermoelectric materials. *Microstructures* **2025**, 5, 2025075-2025093. DOI: 10.20517/microstructures.2024.134

50. An, W.; Wang, H.; Yang, T.; Xu, J.; Wang, Y.; Liu, D.; Hu, J.; Cui, W.; Liang, Y. Enriched photocatalysis-Fenton synergistic degradation of organic pollutants and coking wastewater via surface oxygen vacancies over Fe-BiOBr composites. *Chem. Eng. J.* **2023**, 451, 138653-138665. DOI: 10.1016/j.cej.2022.138653.

51. Cancino-Moreno, A. D.; López-Marure, A.; Arellano-Ahumada, S. N.; Ramírez-Rosales, D.; García-Hernández, M. Correlation of EPR and Photoluminescence Analysis for Crystalline Defects in Eu^{3+}/Yb^{3+}-Doped Lutetium Silicate Sol-Gel Powders. *Inorganics* **2025**, 13 (11), 343-353. DOI: 10.3390/inorganics13110343.

52. Liu, J.; Xiang, Y.; Chen, Y.; Zhang, H.; Ye, B.; Ren, L.; Tan, W.; Kappler, A.; Hou, J. Quantitative Contribution of Oxygen Vacancy Defects to Arsenate Immobilization on Hematite. *Environ. Sci. Technol*. **2023**, 57 (33), 12453-12464. DOI: 10.1021/acs.est.3c03441.

53. Sang, T.; Zhong, Y.; Hu, C.-H.; Wang, D.-H.; Huang, T.; Jiang, S.; Liu, H.; Wang, W.-Y.; Wei, N.-N. Grey $SrCu_2O_2$ with vacancy and pore structure: Dual organic degradation properties and first-principles calculations. *J. Mol. Struct*. **2024**, 1314, 138678-138689. DOI: 10.1016/j.molstruc.2024.138678

54. Zhu, S.; Chen, S.; Zhang, H.; Yu, W.; Tian, Y.; Hu, X.; Hussain, S.; Lin, L.; Chen, W.; Xu, C. Vanadium pentoxide nanosheets with rich oxygen vacancies as a high-performance electrode for supercapacitors. *Ionics* **2022**, 28, 2931-2942. DOI: 10.1007/s11581-022-04541-3

55. Ji, Y.; Xia, M.; Wang, H.; Yao, W. Defect-driven piezocatalysis in zinc

hydroxystannate: Role of oxygen vacancies and interfaces. *Mater. Today Commun*. **2025**, 44, 112046-112054. DOI: 10.1016/j.mtcomm.2025.112046

56. Benavides-Guerrero, J. A.; Gerlein, L. F.; Angel-Ospina, A. C.; Fourmont, P.; Bhattacharya, A.; Zirakjou, A.; Vaussenet, F.; Ross, C. A.; Cloutier, S. G. Room-temperature laser crystallization of oxygen vacancy-engineered zirconia for additive manufacturing. *Addit. Manuf.* **2025**, 111, 104969-104979. DOI: 10.1016/j.addma.2025.104969

57. Luo, Z.; Li, X.; Wang, X.; et al. The langasite family for the development of oxygen-vacancy-mediated oxide ion conductors. *Chem. Mater.* **2024**, 36, 2835-2845. DOI: 10.1021/acs.chemmater.3c03148